Visual Abstract

Method for locating weak zones at coal-bed–host rock interface in the context of outburst hazard: Theory and laboratory experiment

Larisa Nazarova, Leonid Nazarov
Chinakal Institute of Mining of the Siberian Branch of the RAS, Novosibirsk, Russia
larisa.a.nazarova@mail.ru, http://orcid.org/0000-0002-3712-2939
mining1957@mail.ru, http://orcid.org/0000-0002-9857-295X

ABSTRACT. Within the framework of a geomechanical model that describes deformation of rock mass during extraction of subhorizontal coal beds, the outburst hazard mechanism is substantiated: the approach of a working face to a weak zone at the coal-bed–host rock interface initiates tensile stress areas, which creates the prerequisites for the face spalling and loss of coal with methane. The inverse problem of determining conditions at the horizontal boundaries of a coal bed is formulated and solved using tomography data (patterns of P-wave velocity V) and the empirical dependence of V on the mean normal stress σ.

Lab-scale test results on stepwise compression of parallelepipeds made of artificial geomaterials are presented. Tomography of the specimens was performed by acoustic sounding data, and the pattern of velocities V_* was obtained. Using the pre-found empirical dependence $V(\sigma)$ for geomaterial, the distribution $\sigma_*=V^{-1}(V_*)$ in the specimen was calculated, which served as the input data for the inverse problem on the shear stresses σ_{xy} at the specimen–press plate interface. The inversion of the lab data confirmed the possibility of identifying weak zones at the boundaries where $\sigma_{xy}\approx 0$. These zones are associated with probable sources of failure and outbursts.

KEYWORDS. Coal and rock mass, Lab test, Tomography, Geomaterial, Inverse problem, Outburst.

OPEN ACCESS

Citation: Nazarova, L., Nazarov, L., Method for locating weak zones location at coal-bed–host rock interface in the context of outburst hazard: Theory and laboratory experiment, Frattura ed Integrità Strutturale, 63 (2023) 13-25.

Received: 10.07.2022
Accepted: 02.10.2022
Online first: 16.10.2022
Published: 01.01.2023

INTRODUCTION

The rate of the face advance in longwall mining can reach 20–30 m per day [1, 2], consequently, rock mass experiences rapid changes in geomechanical fields, which can induce rock fracture and hazardous dynamic phenomena (rock bursts, outbursts) [3–5]. The current condition of coal and rock mass is estimated using the data of air/gas ratio control, and microseismic and electromagnetic emission monitoring [6–8], which are recorded by mine control equipment (MMS [9], MineARC [10]). The interpretation of these data towards a short-term forecast of dynamic events includes:

—semi-empirical models (for example, damage accumulation [11]) and statistical space–time analysis of long time series of informative parameters of geodynamic processes (in particular, seismic energy density in the study area) [12–17];

—identification of signs of a dynamic event the initiation mechanism of which is, as a rule, determined from a geomechanical model [18–21].

Seismic tomography [22–24] is recently often used in assessment of rock mass condition; in this case, areas of increased elastic wave velocities are associated with the stress concentration zones which are potential sources of dynamic events. A method for quantifying the external field stresses based on passive tomography data was proposed [25].

The passive methods are disadvantageous in monitoring induced seismicity parameters as they are deficient even for a medium-term forecast to be made or for detecting areas of concern located outside the illuminated domain in the object under study.

In ore mining [26] and in extraction of coal [27, 28], most of the dynamic events are associated with discontinuities (faults, dikes) which disturb the stress state of the rock mass. The interfaces of coal beds and host rocks play the same role. Some sites of these interfaces represent thin interburdens of carbonaceous rocks or high-ash clayey coals [29, 30] with low deformation characteristics and strength properties (for example, cohesion of 0.005–0.2 MPa [31, 32]). When the mining front approaches such sites, the stresses change abruptly and the dynamic events take place [27, 33, 34]. Early detection of such weak zones will enable preventive measures to be undertaken [35] to reduce the risk of the undesirable geodynamic phenomena.

In this article, a method for detecting weak zones is proposed and tested on a laboratory scale. The method includes solution of the inverse boundary value problem for shear stresses at the coal-bed–host rock interface using the tomography data. Perhaps, this will allow us to see into one of the "rock mechanics enigma" [36].

GEOMECHANICAL MODEL OF THE OBJECT

Longwall mining technology

Longwall mining is one of the most effective methods for extracting coal beds of various thickness (from thin, up to 1 m to high coal, more than 5-6 m). First, a coal bed is divided into extraction panels (lateral dimensions about 1–2 km) which, in turn, are then cut into rectangular sub-panels (Fig. 1). The sub-panel dimensions can range widely (length l_p from 20 to 200 m, width w_p from 20 to 100 m) depending on the geological structure of the deposit and on the productivity of the coal cutter–loader [37]. With such dimensions, the stress state of the sub-panel in the vertical sections (dashed line in Fig. 1) can be described in terms of the plane strain state [38] model if the external stress field corresponds to the normal faulting geodynamic regime [39].

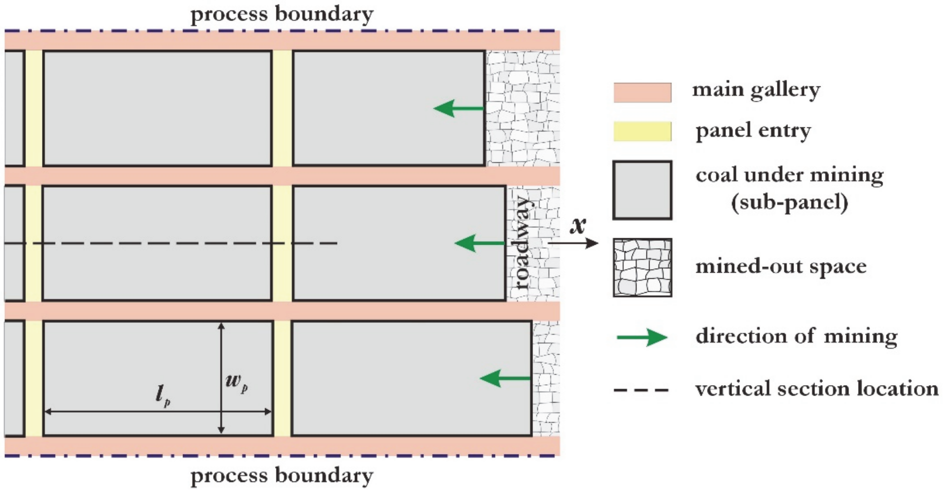

Figure 1: Longwall mining layout.

Formulation of direct problem

In the Cartesian coordinate system (x,y), we consider a vertical section (Fig. 1) of rock mass containing a horizontal coal bed with a thickness $2H$ occurring at a depth D, cut into sub-panels with a length $2L$ by the main galleries and panel entries (Fig. 2). As was stated earlier, we accepted the plane strain hypothesis. The coal bed has a uniform contact with host rock (displacements are continuous), except for four symmetrically located sites with a length $2l$ in the roof and floor, where there is no edge friction. Hereinafter, these sites are called weak zones (WZ).

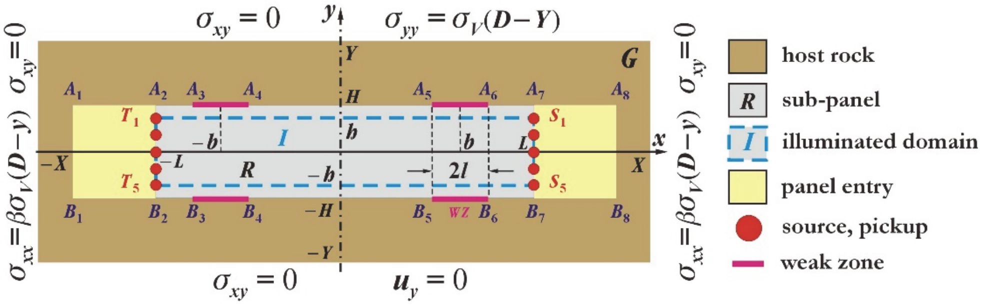

Figure 2: Computational domain and boundary conditions ($\pm b$ are the abscissas of the WZ midpoints).

The stress-strain state in the computational domain $G=\{|x|\le X,\ |y|\le Y\}$ is described by the linear elasticity model including:
the equilibrium equations

$$\sigma_{ij,j}+\varrho g\delta_{iy}=0\,; \tag{1}$$

Hooke's law

$$\sigma_{ij}=\lambda(\varepsilon_{xx}+\varepsilon_{yy})\delta_{ij}+2\mu\varepsilon_{ij} \tag{2}$$

and the Cauchy relations for infinitesimal strains

$$\varepsilon_{ij}=0.5(u_{i,j}+u_{j,i}) \tag{3}$$

where σ_{ij} and ε_{ij} are the components of the stress and strain tensors, respectively; u_i are the displacements ($i,j=x,y$); δ_{ij} is the Kronecker delta; λ, μ and ϱ are the Lamé parameters and rock density; g is the acceleration due to gravity; summation is performed over repeated coefficients. The following boundary conditions are set at different segments of ∂G (Fig. 2):

$$\begin{gathered}
\sigma_{xy}(x,Y)=0,\quad \sigma_{yy}(x,Y)=\sigma_V(D-Y)\\
\sigma_{xy}(x,-Y)=0,\quad u_y(x,-Y)=0\\
\sigma_{xx}(\pm X,y)=\beta\sigma_V(D-y),\quad \sigma_{xy}(\pm X,y)=0\\
\sigma_{xx}=\sigma_{xy}=0\quad on\ A_1B_1,\,A_2B_2,\,A_7B_7\ and\ A_8B_8\\
\sigma_{xy}=\sigma_{yy}=0\quad on\ A_1A_2,\,B_1B_2,\,A_7A_8\ and\ B_7B_8\\
\left[\sigma_{yy}\right]=0\quad on\ A_2A_7\ and\ B_2B_7\\
\left[\sigma_{xy}\right]=0\quad on\ A_2A_3,\,B_2B_3,\,A_4A_5,\,B_4B_5,\,A_6A_7\ and\ B_6B_7\\
\sigma_{xy}=0\quad on\ A_3A_4,\,B_3B_4,\,A_5A_6\ and\ B_5B_5
\end{gathered} \tag{4}$$

where $\sigma_V(y)=\varrho gy$ is the lithostatic stress; β is the lateral pressure coefficient, the symbol [ ] means the jump.

Implementation of system (1)–(4) used the finite element method on a square grid (x_m, y_n) (step of grid is 0.1 m) and an original code [40]. The preset values of the geometric parameters in the model were: L=10 m, H=2 m, l=1 m, D=500 m, X=100 m, Y=20 m. Most of the coal deposits in Kuzbass occur in the regions dominated by the normal faulting regime [41]; therefore, β=0.4 is assumed [38]. Tab. 1 gives the physical properties of rocks according to [42, 43].

Rock	E, GPa	ν	λ, GPa	μ, GPa	ϱ, kg/m^3	σ_t, GPa
Host rock	35	0.25	14	14	2000	5–20
Coal	6	0.21	1.67	2.5	1500	1.0–1.2

Table 1: Physical properties of rocks (E—Young modulus, ν—Poisson ratio, σ_t—tensile strength).

Outburst mechanism

Fig. 3 shows the minimum principal stress pattern

$$\sigma_2 = \frac{1}{2}\left(\sigma_{xx} + \sigma_{yy} - \sqrt{(\sigma_{xx} - \sigma_{yy})^2 + 4\sigma_{xy}^2}\right)$$

in the coal bed at different distances between WZ and the roadway: the positive values correspond to compression and the negative values—to tension. If there is no WZ (Fig. 3a), then a tensile stress area appears in the vicinity of the roadway, and σ_2 in this area is much less than σ_t. A similar situation occurs in the coal bed if the roadway comes short of WZ (Fig. 3b, b=8 m). A qualitatively different picture is observed when the roadway crosses the weak zone (Fig. 3c, b=9 m): an area of tensile stresses appears in the vicinity of WZ, and the magnitude of these stresses exceeds the tensile strength of coal. Taking into account the presence of free gas in the coal bed, these areas are the most probable sources of outbursts [44], when separation failure occurs and coal bursts into the roadway.

Early detection of WZ will enable preventive measures to be undertaken (for example, pre-drilling) to reduce the risk of dynamic events.

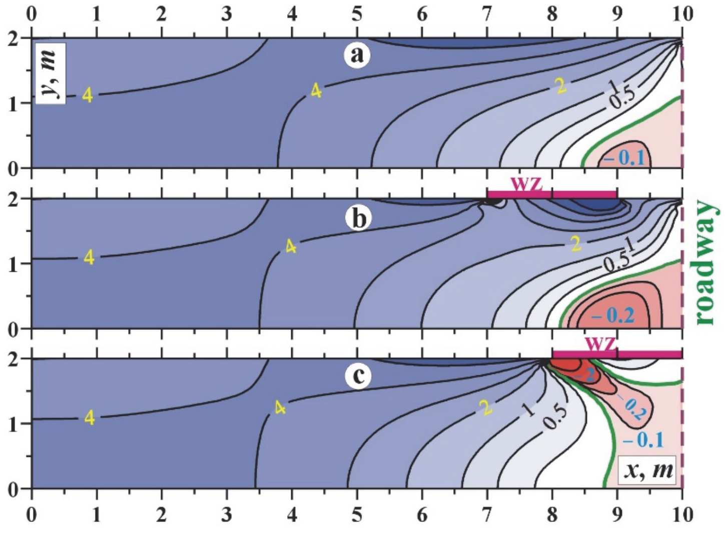

Figure 3: Isolines of principal stress σ_2 (MPa) in coal bed at different locations of WZ relative to roadway.

Formulation and solution of inverse problem for detecting weak zones

The velocity of elastic waves in rocks depends on stresses [45, 46]. Weak zones at the coal-bed–host rock interface perturb the stress field (Figs. 3b and 3c). These perturbations affect the wave velocities, thus, it is possible to use the acoustic tomography data of the coal bed to reconstruct the stress state and locate the WZ.

The dependence of the P-wave velocity V in hard coal on the mean normal stress σ can be described by the empirical relation

$$V(\sigma) = A_0 - B_0 \exp(-a\sigma) \tag{5}$$

where A_0=2698 m/s, B_0=484 m/s, a=0.0779 1/MPa [47].

Fig. 4 depicts the velocities V in the sub-panel at different distances between WZ and the roadway (solid lines—b=8 m, dashed lines—b=6 m), calculated by model (1)–(4) with regard to (5) and at the mean normal stress $\sigma=(1+\nu)(\sigma_{xx}+\sigma_{yy})/3$ as per the plane strain conditions. Apparently, the velocity fields in the vicinity of WZ have a noticeable difference detectable using seismic tomography if the first break times are determined with an absolute accuracy of no less than 0.1 ms (spatial resolution 0.2 m).

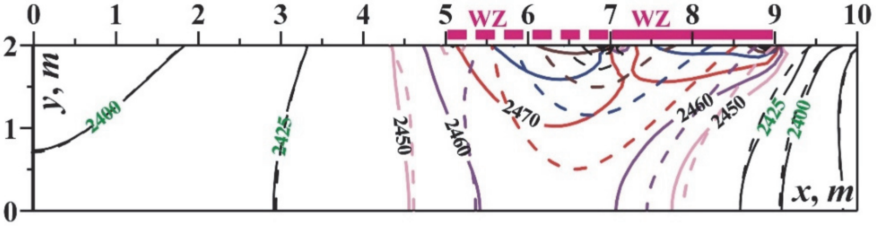

Figure 4: Isolines of P- wave velocity V (m/s) in coal bed at different locations of WZ.

We formulate the inverse boundary value as follows: at the known vertical stresses $\sigma_{yy}(x,H)=F_y(x)$ in the coal bed roof, we find the shear stresses $\sigma_{xy}(x,H)=F_x(x)$ if the distribution of P-wave velocities in the illuminated domain I (Fig. 3) is known at a given shooting scheme. The roof and floor sites where $\sigma_{xy}(x,H)\approx 0$ are associated with WZ. This formulation is allowable since the distribution of the abutment pressure in subhorizontal coal mining can be found *a priori* (based on the configuration of mined-out space and rock density), while the conditions at the coal-bed–host rock interface are usually unknown [5, 30, 48].

Let us generate input data for the inverse problem. For a certain value of b and the above parameters of model (1)–(4) in the region $R=\{|x|\le L, |y|\le H\}$ (Fig. 2), we calculate the stresses and then, using (5), the distribution of P-wave velocities $V_0(x,y)$. In the domain $I=\{|x|\le L, 1\le y\le 3\}$, we define a shooting scheme that includes five sources S_q (q=1,…,5) and receivers T_p (p=1,…,5) at the vertical boundaries of the sub-panel (red circles in Fig. 2). Based on $V_0(x,y)$, we calculate the first break times t^0_{pq} to be later on imposed with the multiplicative noise with the magnitude δ=0.1 ms

$$t^*_{pq} = (1+\delta\xi)t^0_{pq},$$

where ξ is a random variable uniformly distributed over [-1,1]. Using the original code [49], we perform tomography by $\{t^*_{pq}\}$, find the distribution of the velocities $V_*(x,y)$ in the illuminated domain I (Fig. 5) and, finally, from (5), obtain the input data

$$\sigma_*(x,y) = \frac{1}{a}\ln\frac{B_0}{A_0 - V_*(x,y)}. \tag{6}$$

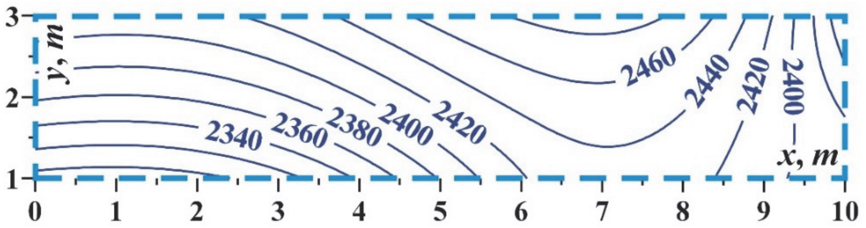

Figure 5: Synthesized P-wave velocity V_* distribution.

In the domain G of the finite element grid, we select a fragment corresponding to the extraction sub-panel R (Fig. 2). For each element of the set $\{x_{m_1}=-L, x_{m_1+1},\dots,x_{m_2}=L\}$, we set the conditions at ∂R for (1)–(3)

$$\sigma_{xy}(x,\pm H)=\pm f_m(x), \quad \sigma_{yy}(x,\pm H)=F_y(x) \tag{7}$$

$$\sigma_{xx}(\pm L,y)=\sigma_{xy}(\pm L,y)=0,$$

where

$$f_m(x)=\begin{cases}1 & x=x_m\\ 0 & x\neq x_m\end{cases}.$$

The set $\{\sigma_{ij}^m(x,y)\}_{m=m_1,\dots,m_2}$ of solutions of system (1)–(3), (7) is discrete Green's function for the boundary value problem:

$$\sigma_{xy}(x,H)=F_x(x), \quad \sigma_{yy}(x,H)=F_y(x)$$

$$\sigma_{xy}(x,-H)=-F_y(x), \quad \sigma_{yy}(x,-H)=F_y(x)$$

$$\sigma_{xx}(\pm L,y)=\sigma_{xy}(\pm L,y)=0$$

We represent the function $\boldsymbol{F_x}$ as a sum

$$F_x(x)=\sum_{m=m_1}^{m_2} C_m f_m(x) \tag{8}$$

with unknown coefficients C_m which are determined by the LS method from the condition of the cost function minimum

$$\Phi(C_{m_1},\dots,C_{m_2})=\iint\limits_I\left[\sum_{m=m_1}^{m_2} C_m\sigma^m(x,y)-\sigma_*(x,y)\right]^2 dxdy\rightarrow min \tag{9}$$

where

$$\sigma^m(x,y)=(1+\nu)(\sigma_{xx}^m+\sigma_{yy}^m)/3.$$

A system of linear equations with respect to C_m can be derived from (9)

$$\sum_{m=m_1}^{m_2} K_{nm}C_m=Q_n \tag{10}$$

$$K_{mn}=\iint\limits_I \sigma^m(x,y)\sigma^n(x,y)dxdy\,,\ Q_n=\iint\limits_I \sigma_*(x,y)\sigma^n(x,y)dxdy\,,\ n=m_1,\dots,m_2\,.$$

Solution of (10) together with (8) gives the desired distribution of the shear stresses $\sigma_{xy}(x,H)=F_x(x)$ at the boundary of the extraction sub-panel.

The red dashed line (Fig. 6) shows the exact distribution of $\sigma_{xy}(x,H)$ at b=7 m, and the blue solid line shows the result of the inverse problem solution using the described procedure—the reconstructed function $F_x(x)$ which clearly indicates the existence of a weak zone in the section $6\leq x\leq 8$.

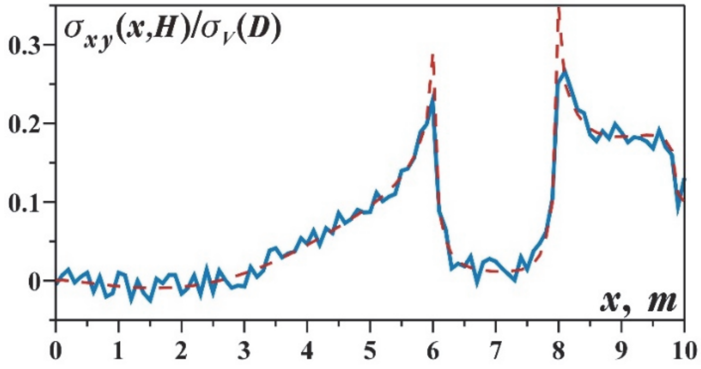

Figure 6: Exact and reconstructed shear stresses at sub-panel boundary.

LABORATORY EXPERIMENT

To test the proposed approach to assessing shear stresses at the coal-bed–host rock interface using tomography, a laboratory experiment was carried out using non-standard specimens.

Model geomaterial

The main goal of the laboratory experiments was to test the usability of acoustic methods in detection of WZ on contact surfaces in high-stress coal and rock mass under conditions close to real life (the empirical dependence of velocities on stresses corresponds to coal). In this regard, the epoxy resin + mica composition was chosen as a model material. The percentage of mica was selected so that the acoustic and deformation characteristics of the manmade geomaterial corresponded to coal of medium hardness. Five cylindrical specimens (height 76 mm, diameter 38 mm) were manufactured, and the three specimens (without mica) were tested in uniaxial compression according to the standard procedure [50]. The P-wave velocity V was also determined by acoustic sounding. Tab. 2 offers the results obtained (mean values).

E, GPa	ν	λ, GPa	μ, GPa	ρ, kg/m^3	V, m/s
9.2	0.21	2.76	3.8	1600	2350

Table 2: Physical properties of epoxy resin.

The other two specimens (with different mica contents) were subjected to stepwise axial loading, and the P-wave velocity V was determined by ultrasonic sounding at each stress σ_1. The data obtained (Tab. 3) were approximated by the exponential function (5), the values of the empirical constants A_0, B_0 and a were found by the least square method, and $\sigma=(1+\nu)\sigma_1/3$. These values were used for the experimental data interpretation.

Specimen	σ_1, MPa							A_0 m/s	B_0 m/s	a 1/MPa
	0	1	2	3	4	5	6			
1	1710	1750	1790	1825	1860	1890	1910	2046	325	0.1263
2	1740	1790	1840	1875	1905	1925	1950	2091	342	0.1412

Table 3: Stress dependence of P-wave velocity V (m/s).

Laboratory setup and experimental design

For the main experiments, four specimens were manufactured in the form of a parallelepiped with dimensions: length L=100 mm, height H=140 mm, thickness 30 mm (Fig. 7). A specimen was placed in a loading machine (Instron 300DX, maximum force 300 kN), thin silicone plates (length l) were embedded between the specimen and plates P_1 and P_2 (Figs.

7, 8) in order to simulate WZ. Six piezoelectric transducers $T_1,\ldots,T_6$, $S_1,\ldots,S_6$ (operating frequency 60–70 kHz) were arranged on the vertical faces of the specimen to function as sources and receivers. Fig. 9 shows general view photo of the laboratory setup.

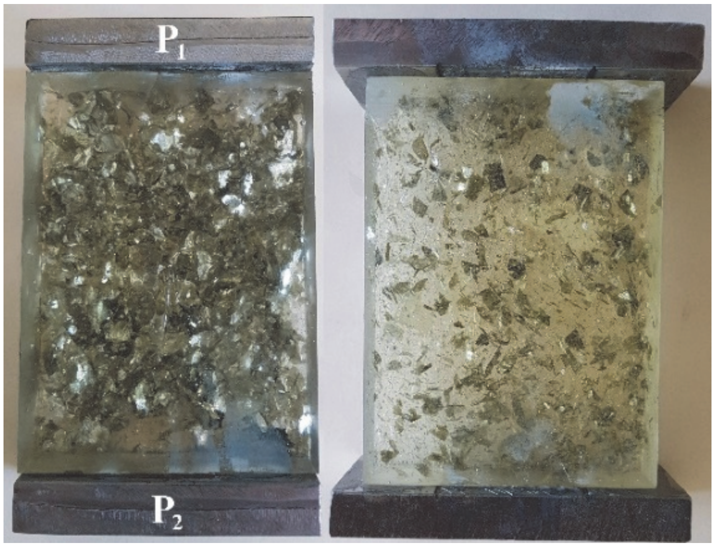

Figure 7: Parallelepiped-shaped specimens of manmade geomaterial.

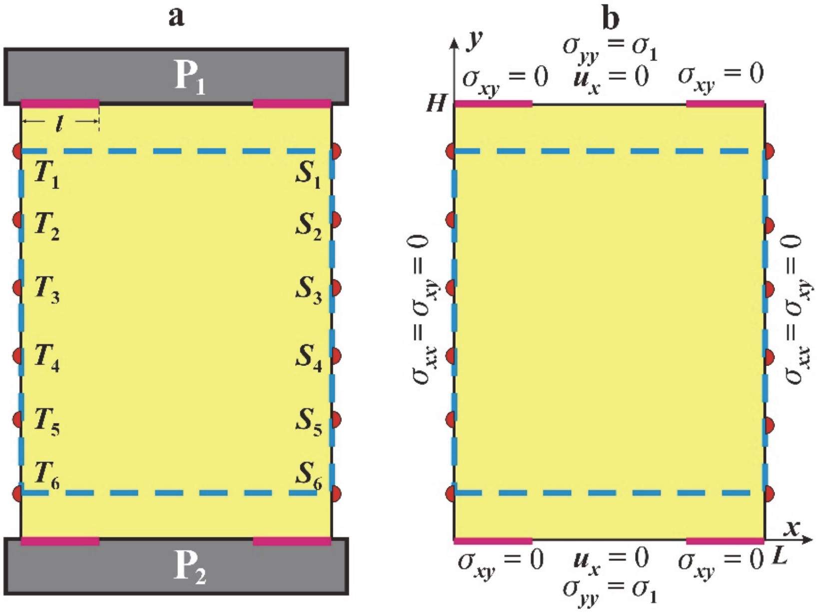

Figure 8: Experimental design and shooting geometry (a); computational domain and boundary conditions for lab data inversion (b).

The specimen was subjected to vertical incremental loading at a step of 3 MPa. Sounding was carried out at each loading stage k: one of the sources generated a pulse received by six transducers on the opposite face, and the absolute recording accuracy was 0.1 μs (ADC frequency is 10 MHz). By the first break, the P-wave travel time t^k_{pq} between the sensors T_p and S_q (p,q=1,…,6) was determined as an average value over ten soundings. The set $\{t^k_{pq}\}$ is the input data for the specimen tomography.

Two series of experiments included measurement of the wave travel times at the vertical stresses σ_1=3 and 6 MPa if: the plates were rigidly connected with the specimen (l=0); at the specimen–plate interfaces, there were low friction areas (WZ) with the length l=25 mm (thick red lines in Fig. 8). By way of illustration, Tab. 4 gives the values of t^k_{pq} in the presence of WZ.

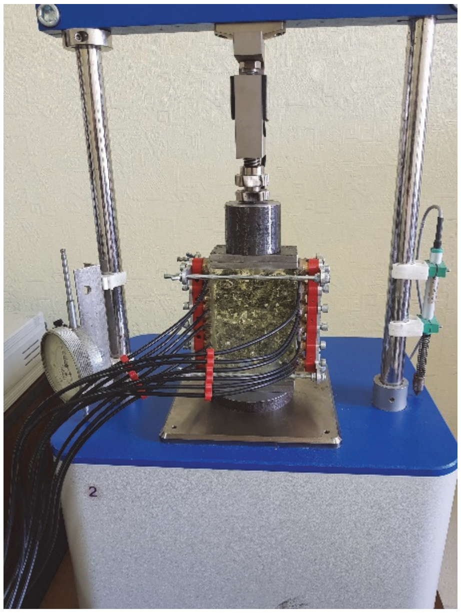

Figure 9: General view of laboratory setup.

	σ_1=3 MPa (k=1)						σ_1=6 MPa (k=2)					
	T_1	T_2	T_3	T_4	T_5	T_6	T_1	T_2	T_3	T_4	T_5	T_6
S_1	56.5	57.9	61.8	67.8	75.5	84.2	55.3	56.6	60.5	66.4	73.8	82.4
S_2	57.9	56.6	58.0	61.9	67.9	75.4	56.6	55.3	56.7	60.5	66.4	73.8
S_3	61.8	57.9	56.6	58.0	61.9	67.8	60.5	56.7	55.4	56.7	60.5	66.3
S_4	67.8	61.8	57.9	56.6	58.0	61.8	66.3	60.5	56.7	55.4	56.7	60.4
S_5	75.3	67.8	61.8	57.9	56.6	57.9	73.7	66.3	60.5	56.7	55.3	56.6
S_6	84.1	75.3	67.8	61.8	57.9	56.5	82.2	73.7	66.3	60.5	56.6	55.3

Table 4: P-wave travel times t_{pq}^{k} (μs) between sensors.

Experimental data interpretation

The tomography of the specimens was carried out by the times t_{pq}^{k} using algorithm [49]. Fig. 10 presents the reconstructed field of the P-wave velocities V_* in the illuminated domain (blue dash line rectangle in Fig. 8) with the selected observation system $\{T_p, S_q\}$ at σ_1=6 MPa and the weak zones at the interfaces of the specimen and loading plates. The main cause for the asymmetry of the $V_*(x,y)$ isolines is the random arrangement of the filler particles in the specimens (Fig. 7). For this reason, for example, the travel times t_{16}^{1} and t_{61}^{1} (Tab. 4) turn out to be different, although distances between the corresponding sensors are the same, and the loading is symmetrical about two axes x=0.5L and y=0.5H.

To find the shear stresses σ_{xy} at the horizontal boundaries of the domain $G=\{0\le x\le L,\ 0\le y\le H\}$ (Fig. 8b), we formulate the boundary value problem for the system of Eqns. (1)–(3):

$$\sigma_{xy}(x,H)=F_x(x),\quad \sigma_{yy}(x,H)=\sigma_1$$

$$\sigma_{xy}(x,0)=-F_x(x),\quad \sigma_{yy}(x,0)=\sigma_1$$

$$\sigma_{xx}(0,y)=\sigma_{xy}(0,y)=\sigma_{xx}(L,y)=\sigma_{xy}(L,y)=0$$

corresponding to the experimental conditions. The unknown function F_x is found using the procedure for solving the boundary inverse problem described in the previous section of the article. The input data are the mean normal stress distributions σ_* in the illuminated domain, found from the reconstructed velocity fields V_* (Fig. 9) with regard to (6) and the values A_0, B_0 and a (Tab. 3, line 1). Fig. 10 presents the calculated results which indicate that the curves $F_x(x)$ clearly identify WZ—the boundary sites $0\le x/L\le 0.25$ and $0.75\le x/L\le 1$ where $F_x(x)\approx 0$.

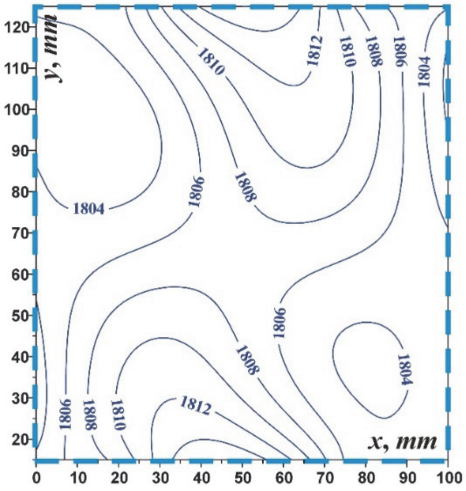

Figure 9: P-wave velocities V_* (m/s) in specimen illuminated domain, restored from tomography by t_{pq}^{2} at σ_1=6 MPa and l=25 mm.

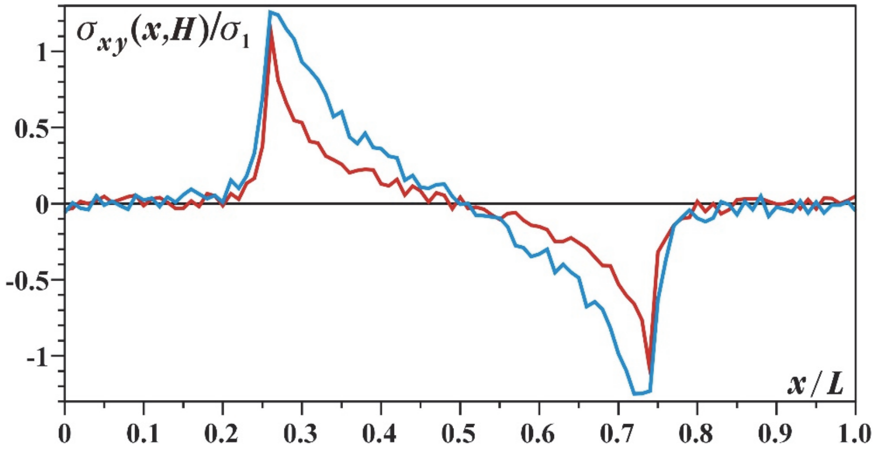

Figure 10: Shear stress σ_{xy} on the upper face of the specimen under different vertical loads (red line—σ_1=3 MPa, blue line—σ_1=6 MPa) found from solving inverse problem by tomography data t_{pq}^{k} .

CONCLUSIONS

The method for determining conditions at the coal-bed–host rock interface has been theoretically substantiated and experimentally validated. It relies on solving an inverse boundary value problem within the framework of a geomechanical model by seismic tomography data using empirical dependences of elastic wave velocity on stresses obtained in a laboratory setting. The method not only permits to reconstruct the stress state of rock mass in the course of mining, but also acts as an element of a system for predicting outbursts in extraction of subhorizontal bedded coal.

It appears that further investigations should develop in two directions: extending the proposed approach to locating zones of concern in a three-dimensional case; use of microseismic emission to improve the resolution of tomography.

ACKNOWLEDGMENTS

The study was carried out within R&D Project, State Registration Number 121062200075-4. The authors would like to express gratitude to the colleagues from the MISIS National University of Science and Technology (Moscow) for the support.

REFERENCES

[1] Wang, X., Ding, W. and Tan, G. (2016). Adaptability evaluation of fully mechanized coal mining under the condition of typical coal seam, J. of Measurements in Engineering, 4(4), pp. 209–216. DOI: 10.21595/jme.2016.17888.
[2] Zakharov, V.N., Malinnikova, O.N. and Averin, A.P. (2016). Modeling of vibrational-oscillatory processes in the face space of a coal-rock mass under technogenic impact, Gornyi Zhurnal, 12, pp. 28–32. DOI: 10.17580/gzh.2016.12.06.
[3] Seidle, J. (2011). Foundations of Coalbed Methane Reservoir Engineering, Tulsa, PennWell Books.
[4] Singh, R.D. (2005). Principles and Practices of Modern Coal Mining, New Delhi, New Age International.
[5] Galvin, J.M. (2016). Ground Engineering – Principles and Practices for Underground Coal Mining, Switzerland, Springer International Publishing. DOI: 10.1007/978-3-319-25005-2.
[6] Ge, M. (2005). Efficient mine microseismic monitoring, Int. J. of Coal Geology, 64(1–2), pp. 44-56. DOI: 10.1016/j.coal.2005.03.004.
[7] Pandit, V. and Rane, U.A. (2013). Design of underground coal mine monitoring system, Int. J. of Engineering Research and Technology, 2(5), pp. 83–90. DOI: 10.17577/IJERTV2IS50141.
[8] Zhenbi, L. and Baiting, Zh. (2012). Microseism monitoring system for coal and gas outburst, Int. J. of Computer Science Issues, 5(1), pp. 24–28.
[9] Ma, T., Lin, D., Tang, C. et al. (2020). Microseismic monitoring, positioning principle, and sensor layout strategy of rock mass engineering, Geofluids, 2020, Article ID 8810391. DOI: 10.1155/2020/8810391.
[10] Available at: https://minearc.com/products/mining-equipment.
[11] Kuksenko, V.S., Makhmudov, K.F. and Manzhikov B. Ts. (2010). Damage accumulation model for solids and the catastrophy prediction for large-scale objects, J. of Mining Science, 46(4) pp. 384–393. DOI: 10.1007/s10913-010-0048-z.
[12] Morgen, R., Leake, W.J., Conrad, E.C. et al. (2017). Microseismic monitoring and analysis of induced seismicity source mechanisms in a retreating room and pillar coal mine in the Eastern United States, Underground Space, 2(2), pp. 115–124. DOI: 10.1016/j.undsp.2017.05.002.
[13] Zhang, H., Song, W., Yang, H. and Zhang, M. (2008). Pattern recognition prediction of coal and gas outburst hazard in the sixth mine of Hebi, J. of Coal Science and Engineering, 14(2), pp. 248–251. DOI: 10.1007/s12404-008-0052-y.
[14] Zhou, B., Xu, J., Yan, F. et al. (2021). Effects of gas pressure on dynamic response of two-phase flow for coal-gas outburst, Powder Technology, 377, pp. 55–69. DOI: 10.1016/j.powtec.2020.08.065.
[15] Li, X.L., Wang, E.Y., Li, Z.H. et al. (2016). Rock burst monitoring by integrated microseismic and electromagnetic radiation methods, Rock Mechanics and Rock Engineering, 49(11), pp. 4393–4406. DOI: 10.1007/s00603-016-1037-6.
[16] Cai, W., Dou, L., Si, G. et al. (2019). A new seismic-based strain energy methodology for coal burst forecasting in underground coal mines, Int. J. of Rock Mechanics and Mining Sciences, 123, 104086. DOI: 10.1016/j.ijrmms.2019.104086.
[17] Zhang, Q. and He, S. (2021). Study on rock burst early warning in the working face of deep coal mines based on the law of gas emission, Advances in Civil Engineering, 2021, Article ID 9940505. DOI: 10.1155/2021/9940505.
[18] Zhang, J.F., Jiang, F.X., Yang, J.B. et al. (2017). Rockburst mechanism in soft coal seam within deep coal mines, Int. J. of Mining Science and Technology, 27(3), pp. 551–556. DOI: 10.1016/j.ijmst.2017.03.011.
[19] Wang, G., Gong, S., Dou, L. et al. (2019). Rockburst mechanism and control in coal seam with both syncline and hard strata, Safety Science, 115, pp. 320–328. DOI: 10.1016/j.ssci.2019.02.020.
[20] He, L.M., Dou, S.Y., Gong, J. et al. (2017). Rock burst assessment and prediction by dynamic and static stress analysis based on micro-seismic monitoring, Int. J. of Rock Mechanics and Mining Science, 93, pp. 46–53. DOI: 10.1016/j.ijrmms.2017.01.005.

[21] Cao, W., Shi, J.-Q., Si, G. et al. (2018). Numerical modelling of microseismicity associated with longwall coal mining, Int. J. of Coal Geology, 193, pp. 30–45. DOI: 10.1016/j.coal.2018.04.010.

[22] Luxbacher, K., Westman, E., Swanson, P. and Karfakis, M. (2008). Three-dimensional time-lapse velocity tomography of an underground longwall panel, Int. J. of Rock Mechanics and Mining Science, 45, pp. 478–485. DOI: 10.1016/j.ijrmms.2007.07.015.

[23] Gong, S.Y., Li, J., Ju, F. et al. (2019). Passive seismic tomography for rockburst risk identification based on adaptive-grid method, Tunneling and Underground Space Technology, 86, pp. 198–208. DOI: 10.1016/j.tust.2019.01.001.

[24] Dou, L.M., Chen, T.J., Gong, S.Y. et al. (2012). Rockburst hazard determination by using computed tomography technology in deep workface, Safety Science, 50(4), pp. 736–740. DOI: 10.1016/j.ssci.2011.08.043.

[25] Nazarova, L.A., Zakharov, V.N., Shkuratnik, V.L. et al. (2017). Use of tomography in stress-strain analysis of coal-rock mass by solving boundary inverse problems, Procedia Engineering, 191, pp. 1048–1055. DOI: 10.1016/j.proeng.2017.05.278.

[26] Cai, W., Dou, L., Si, G. and Hu, Y. (2021). Fault-induced coal burst mechanism under mining-induced static and dynamic stresses, Engineering, 7(5), pp. 687–700. DOI: 10.1016/j.eng.2020.03.017.

[27] Li, T., Mu, Z., Liu, G. et al. (2016). Stress spatial evolution law and rockburst danger induced by coal mining in fault zone, Int. J. Mining Science and Technology, 26(3), pp. 409–415. DOI: 10.1016/j.ijmst.2016.02.007.

[28] Konicek, P. and Waclawik, P. (2018). Stress changes and seismicity monitoring of hard coal longwall mining in high rockburst risk areas, Tunneling and Underground Space Technology, 81, pp. 237–251. DOI: 10.1016/j.tust.2018.07.019.

[29] Mironov, K.V. (1988). Handbook of the Geologist-Coal Miner, Moscow, Nedra.

[30] Dorokhov, D.V., Sivokhin, V.I., Kostyuk, I.S. and Podtykalov, A.S. (1997). Technology of Underground Mining of Stratified Deposits of Minerals, Donetsk, DonGTU.

[31] Roof Control and Support in Longwalls on Coal-bed with Dip up to 35°. (2002). Guideline KD 12.01.01.503. 2001. Kyiv: Ministry of Fuel and Energy of Ukraine, DonUGI.

[32] Schuster, R.L. and Turner, A.K. eds, (1996). Rock strength properties and their measurement, In: Landslides: Investigation and Mitigation. Transportation research board, National research council. Special report, 247, Washington, National Academy Press, pp. 372–390.

[33] Sames, G.P. and Moebs, N.N. (1992). Roof control of stress-relief jointing near outcrops in central Appalachian drift coal mines, U.S. Bureau of Mines Information Circular 9313, 11 p.

[34] Zhao, W., Qin, C., Xiao, Z. and Chen, W. (2022). Characteristics and contributing factors of major coal bursts in longwall mines, Energy Science and Engineering, 10(4), pp. 1–14. DOI: 10.1002/ese3.1102.

[35] Brauner, G. (1994). Rockbursts in Coal Mines and their Prevention, London, A.A.Balkema. DOI: 10.1201/9780203740446.

[36] Mark, C. (2018). Coalbursts that occur during development, a rock mechanics enigma, Int. J. Mining Science and Technology, 28, pp. 35–42. DOI: 10.1016/j.ijmst.2017.11.014.

[37] Peng, S.S. (2020). Longwall Mining, London, CRC Press. DOI: 10.1201/9780429260049.

[38] Jaeger, J.G., Cook, N.G.W. and Zimmerman, R.W. (2007). Fundamentals of Rock Mechanics, USA, Blackwell Publishing. DOI: 10.1017/CBO9780511735349.

[39] Nazarova, L.A. (1999). Estimating the stress and strain fields of the earth's crust on the basis of seismotectonic data. J. of Mining Science, 35(1), pp. 26-35. DOI: 10.1007/BF02562442.

[40] Nazarova, L.A. and Nazarov, L.A. (2009). Dilatancy and the formation and evolution of disintegration zones in the vicinity of heterogeneities in a rock mass, J. of Mining Science, 45(5), pp. 411–419. DOI: 10.1007/s10913-009-0052-3.

[41] Heidbach, O., Rajabi, M., Cui, X. et al. (2018). The World Stress Map database release 2016: Crustal stress pattern across scales, Tectonophysics, 744, pp. 484–498. DOI:10.1016/j.tecto.2018.07.007.

[42] Shtumpf, G.G. et al. eds, (1994). Physicotechnical Properties of Coal and Rocks in the Kuznetsk Basin: Reference Book, Moscow, Nedra.

[43] Baron, L.I. and Kerekelitsa, L.G. (1974). The Resistance of Rocks to Separation, Kyiv, Naukova Dumka.

[44] Nazarov, L.A. and Nazarova, L.A. (1999). Some geomechanical aspects of gas recovery from coal seams, J. of Mining Science, 35(2), pp. 135–145. DOI: 10.1007/BF02565367.

[45] Najibi, A.R. and Asef, M.R. (2014). Prediction of seismic-wave velocities in rock at various confining pressures based on unconfined data, Geophysics, 79(4), pp. 235–242. DOI: 10.1190/geo2013-0349.1.

[46] Morcote, A., Mavko, G. and Prasad, M. (2010). Dynamic elastic properties of coal, Geophysics, 75(6), pp. E227–E234. DOI: 10.1190/1.3508874.

[47] Zakharov, V.N., Nazarova, L.A., Protasov, M.I. et al. (2017). Assessment of horizontal external stresses in the Vorkuta mine field using seismic tomography data, J. of Mining Science, 53(6), pp. 993–1000. DOI: 10.1134/S1062739117063053.
[48] Farmer, I.W. (2012). Coal Mine Structures, Switzerland, Springer International Publishing.
[49] Nazarova, L.A., Nazarov, L.A. and Protasov, M.I. (2016). Reconstruction of 3D stress field in coal-rock mass by solving inverse problem using tomography data, J. of Mining Science, 52(4), pp. 623–631. DOI: 10.1134/S1062739116041010.
[50] Ulusay, R. and Hudson, J. eds., (2007). The Complete ISRM Suggested Methods for Rock Characterization, Testing and Monitoring: 1974-2006, Turkey, ISRM Turkish National Group and the ISRM.